www.advmatinterfaces.de

# Perovskite-Based Optoelectronic Biointerfaces for Non-Bias-Assisted Photostimulation of Cells

Mohammad M. Aria, Shashi B. Srivastava, Emine Sekerdag, Ugur M. Dikbas, Sadra Sadeghi, Samuel R. Pering, Petra J. Cameron, Yasemin Gursoγ-Ozdemir, Ibrahim H. Kavakli, and Sedat Nizamoglu\*

Organohalide perovskites have attracted significant attention for efficient solar energy harvesting. They boost the photoelectrical conversion efficiency of the solution-processable solar cells because of having a nearly 100% internal quantum efficiency, operating in both narrow- and broadband spectral regimes, near-infrared sub-bandgap absorption, and high diffusion length. At the same time, these optoelectronic properties make it an ideal candidate for photostimulation of neurons. However, the biocompatibility of perovskite and its longevity in a cell medium constitute a major limitation to use it for biological interfaces. Here, high-level perovskite stability and biocompatibility are shown by forming hydrophobic perovskite microcrystals and encapsulating them within a polydimethylsiloxane layer. For effective and safe photostimulation of cells perovskite microcrystals are interfaced with poly(3-hexylthiophene-2,5-diyl) (P3HT) polymer for dissociation of the photogenerated charge carriers, which leads to non-bias-assisted cell stimulation. The results point out a new direction for the use of perovskite for photomedicine.

1. Introduction

The advancement of neural interfaces has attracted significant attention due to its important role in understanding neuronal

circuits,<sup>[1]</sup> curing neurological diseases, developing neuroprosthetics.<sup>[2]</sup> These interfaces, which utilize different materials and technologies ranging from silicon microelectrodes[3] to nanostructures, [4] have been designed for the treatment of a diverse range of neural diseases such as sensory issues including hearing loss,<sup>[5]</sup> blindness,<sup>[6-8]</sup> spinal cord injury,<sup>[9]</sup> psychiatric diseases,<sup>[10]</sup> and motor disorders.[11] The photoactive interfaces due to their battery-less stimulation mechanism have facilitated many promising health care applications such as retina prosthetics with high-spatial resolution and remote functioning.[8,12,13] Recent studies used semiconductor nanostructures,[14] gold nanoparticles,[15] and hybrid semiconductor polymers[7,12,16] for photoactive neural interfaces. The afore-

mentioned materials showed promising progress for neural prosthetics.

In comparison with the materials used in previous studies, an organohalide perovskite has many unique optoelectronic

M. M. Aria, Prof. S. Nizamoglu Graduate School of Biomedical Sciences and Engineering Koç University

Sariyer, Istanbul 34450, Turkey E-mail: snizamoglu@ku.edu.tr

Dr. S. B. Srivastava, Prof. S. Nizamoglu

Department of Electrical and Electronics Engineering

Koç University

Sariyer, Istanbul 34450, Turkey

E. Sekerdag, Prof. Y. Gursoy-Ozdemir

Neuroscience Research Lab

Research Center for Translational Medicine

Koç University

Istanbul 34450, Turkey

The ORCID identification number(s) for the author(s) of this article can be found under https://doi.org/10.1002/admi.201900758.

© 2019 The Authors. Published by WILEY-VCH Verlag GmbH & Co. KGaA, Weinheim. This is an open access article under the terms of the Creative Commons Attribution-NonCommercial-NoDerivs License, which permits use and distribution in any medium, provided the original work is properly cited, the use is non-commercial and no modifications or adaptations are made.

The copyright line was changed on 27 September 2019 after initial publication.

DOI: 10.1002/admi.201900758

U. M. Dikbas, Prof. I. H. Kavakli Molecular Biology and Genetics

Koç University

Rumeli Feneri Yolu, Sariyer, Istanbul 34450, Turkey

S. Sadeghi

Graduate School of Materials Science and Engineering

Koç University

Sariyer, Istanbul 34450, Turkey

S. R. Pering, Prof. P. J. Cameron

Department of Chemistry

University of Bath

Claverton Road, Bath BA2 7AY, UK

Prof. Y. Gursoy-Ozdemir

Department of Neurology

School of Medicine

Koç University

Istanbul 34450, Turkey

Prof. I. H. Kavakli

Department of Chemical and Biological Engineering

Koç University

Rumeli Feneri Yolu, Sariyer, Istanbul 34450, Turkey

1900758 (1 of 9)

onditions) on Wiley Online Library for rules of use; OA articles are governed by the applicable Creative Commons License



www.advmatinterfaces.de

properties. High absorption coefficient (≈10<sup>4</sup> cm<sup>-1</sup>) covering the whole visible spectrum can be useful to effectively convert the light energy to bioelectrical stimuli.<sup>[17]</sup> Low trap-state densities on the order of 10<sup>9</sup> to 10<sup>10</sup> per cubic centimeter in methylammonium lead trihalide (MAPbX<sub>3</sub>) single crystals<sup>[18]</sup> combined with long diffusion length(up to 175 µm)[19] can enable effective control of the carriers for the designated charge-transfer mechanisms such as Faradaic and capacitive processes. In addition, compositional control varying absorption from ultravoilet (UV) to near-infrared (near-IR) wavelengths<sup>[20]</sup> can lead to spectrally adjustable photoactive substrates. Due to its advantageous properties, a new generation of solution-processable solar cells has experienced a significant improvement in power conversion efficiencies, and ultrasensitive photodetectors has been developed using this material as well. [21-23] However, the stability of the perovskites in ambient conditions still remains as a major challenge, [24] and if we think this unique material in an aqueous environment for biological applications, the stability issue becomes more serious.

The hybrid use of perovskite with organic polymers can enhance its stability.<sup>[25]</sup> Among a wide variety of polymers, P3HT is an ideal polymer, which is biocompatible, durable in biological fluids and can be used as a charge transport layer, [12] and it has been also studied as a photosensitive polymer for neural interfaces.<sup>[7,26]</sup> Here, in this study we employ P3HT in conjunction with perovskite to combine the advantageous properties of the both materials. Furthermore, the intrinsic stability of the perovskite absorber layer is improved via microcrystallization; and poly(dimethylsiloxane) (PDMS), which is a widely investigated in stretchable electronics, microfluidics, robust energy harvesting devices, and bioelectronic implants,<sup>[27]</sup> is used as a durable encapsulation layer on the perovskite and P3HT layer. This crystallization and encapsulation strategy allows for a stable and biocompatible device structure. In addition, the perovskite-P3HT heterojunction leads to a spectral sensitivity that covers from the entire visible toward near-IR. This paradigm-shifting hybrid interface is expected to impact biological interfaces, neural prosthetics,

and the translation of perovskite from physical to healthrelated sciences.

## 2. Results and Discussion

#### 2.1. The Structure of the Biointerface and Its Compatibility

To prepare perovskite photoactive material as a biointerface, stability against water-based degradation is required. The perovskite thin film has a major drawback when it is immersed into water. It gets dissolved by the water and degraded into its constituents, which makes it unstable in aqueous environments (see Figure S1, Supporting Information). Considering the fact of biocompatibility, we prepared perovskite microcrystals by dissolving the precursors in isopropanol solvent (explained in detail in the Experimental Section), which is an environmental-friendly precursor. X-ray diffraction measurement (in Figure 1a) proves the perovskite peaks at 14.15°, 28.49°, 31.94°, and 43.25°  $2\theta$  values, which correspond to (110), (220), (310), and (330) planes of the tetragonal structure of the perovskite. [23,28] Additionally, PbI<sub>2</sub> (001) peak is observed at 12.66°. [29] Scanning electron micrograph (SEM) confirms the perovskite microcrystal formation (Figure 1b). The high roughness and microcrystalline structure lead to a hydrophobic perovskite film, which is confirmed by high water contact angle (Figure 1c).

After perovskite microcrystal confirmation, the perovskite layer is sandwiched between transparent bottom electrode of indium tin oxide (ITO) and hole transport layer of P3HT (Figure 2a). Subsequently, a P3HT:PDMS hybrid layer is deposited on top of the P3HT. The P3HT:PDMS layer (Figure S2, Supporting Information) encapsulates the photoactive layers and circumvents the direct contact of perovskite layer with the neuron cells and its potential toxicity. At the same time, mixing P3HT in PDMS results in better conductivity of the protective layer in comparison with only PDMS layer. The biointerface leads to photon-induced charge generation and dissociation (Figure 2b). The main contribution of the charge generation is

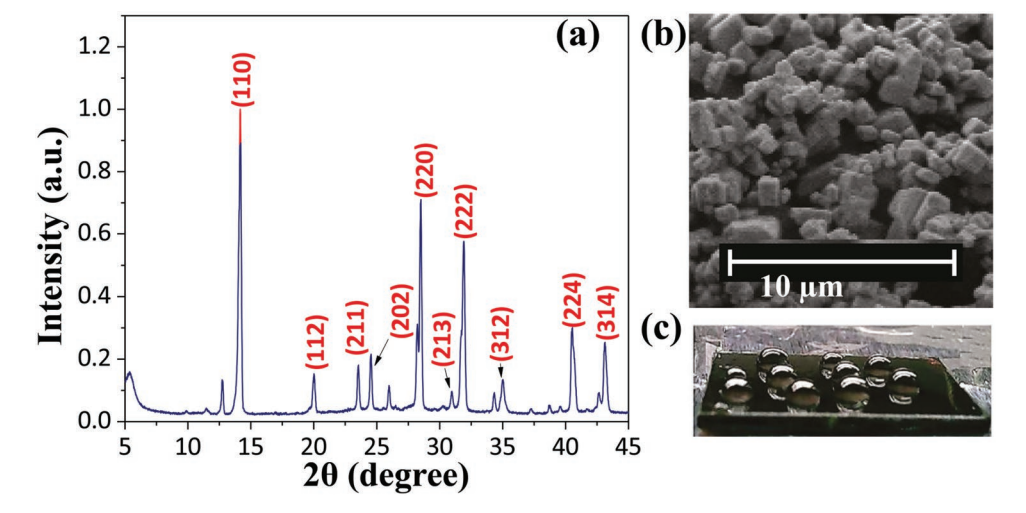


Figure 1. a) X-ray diffraction (XRD) pattern of the ITO/ CH<sub>3</sub>NH<sub>3</sub>PbI<sub>3</sub>/P3HT. b) SEM image of the perovskite microcrystals on ITO substrate. c) Water droplets are placed on the perovskite microcrystals. Water droplets show spherical form due to the hydrophobicity and roughness of the perovskite microcrystals.

Adv. Mater. Interfaces 2019, 6, 1900758

21967350, 2019, 17, Downloaded from https://onlinelibrary.wiley.com/doi/10.1002/admi.201900738 by Egyptian National Sti. Network (Enstinet), Wiley Online Library on [08.03/2023]. See the Terms and Conditions (https://onlinelibrary.wiley.com/doi/10.1002/admi.201900738 by Egyptian National Sti. Network (Enstinet), Wiley Online Library on [08.03/2023]. See the Terms and Conditions (https://onlinelibrary.wiley.com/doi/10.1002/admi.201900738 by Egyptian National Sti. Network (Enstinet), Wiley Online Library on [08.03/2023]. See the Terms and Conditions (https://onlinelibrary.wiley.com/doi/10.1002/admi.201900738 by Egyptian National Sti. Network (Enstinet), Wiley Online Library on [08.03/2023]. See the Terms and Conditions (https://onlinelibrary.wiley.com/doi/10.1002/admi.201900738 by Egyptian National Sti. Network (Enstinet), Wiley Online Library on [08.03/2023]. See the Terms and Conditions (https://onlinelibrary.wiley.com/doi/10.1002/admi.201900738 by Egyptian National Sti. Network (Enstinet), Wiley Online Library on [08.03/2023]. See the Terms and Conditions (https://onlinelibrary.wiley.com/doi/10.1002/admi.201900738 by Egyptian National Sti. Network (https://onlinelibrary.wiley.com/doi/10.1002/admi.20190738 by Egyptian National National National National National National Natio

onditions) on Wiley Online Library for rules of use; OA articles are governed by the applicable Creative Commons License

www.advmatinterfaces.de

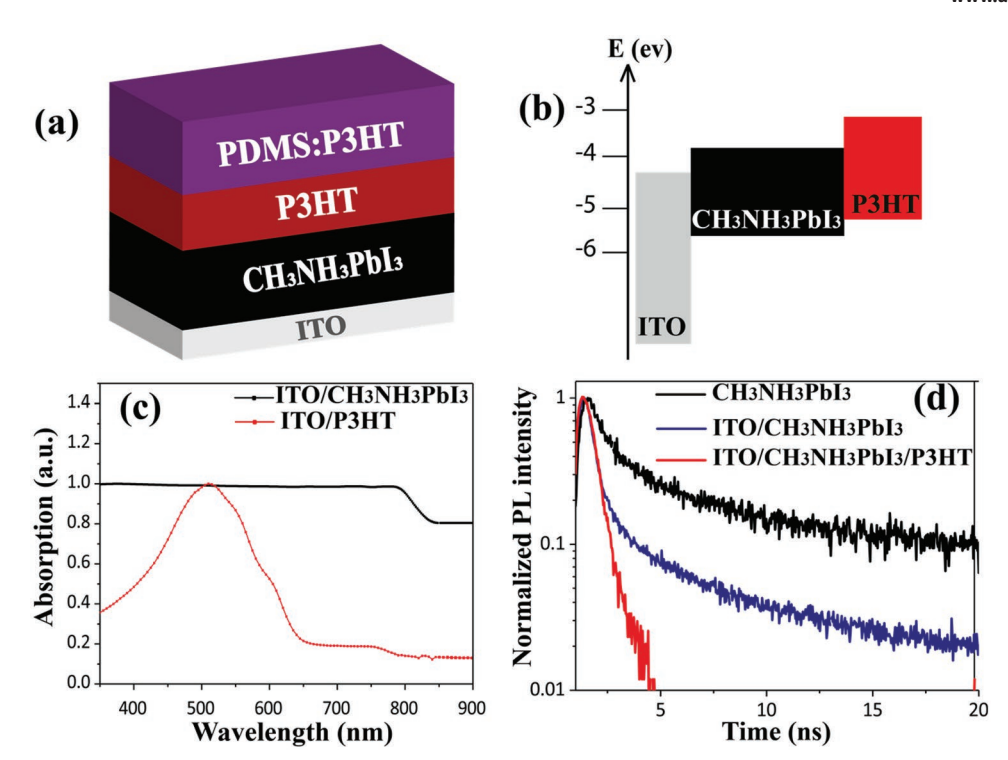


Figure 2. a) Schematic of the biointerface structure. Here, ITO on glass substrate was used as a conductive substrate, the perovskite (CH<sub>3</sub>NH<sub>3</sub>PbI<sub>3</sub>) as a strongly absorbing photoactive layer, P3HT as a biocompatible hole transport layer, and PDMS:P3HT as an encapsulation layer, b) Energy band diagram of the ITO/CH<sub>3</sub>NH<sub>3</sub>PbI<sub>3</sub>/P3HT. c) Absorption spectrum of ITO/P3HT (red dotted line) and ITO/CH<sub>3</sub>NH<sub>3</sub>PbI<sub>3</sub>/P3HT (black dotted line). d) Time-resolved photoluminescence of the perovskite layer on glass, perovskite on ITO (ITO/CH<sub>3</sub>NH<sub>3</sub>PbI<sub>3</sub>), and P3HT on ITO/CH<sub>3</sub>NH<sub>3</sub>PbI<sub>3</sub> (ITO/CH<sub>3</sub>NH<sub>3</sub>PbI<sub>3</sub>/P3HT).

originated by the perovskite layer, which can absorb the entire visible range and near-IR (Figure 2c). Since the biointerface can absorb the entire visible range, the color of the hybrid film under ambient light is black (Figure 1c). After the light is absorbed, the electrons and holes dissociate due to the band structure (Figure 2b), and the photogenerated electrons move toward the ITO side and holes to the P3HT. To further understand the charge transfer mechanism in the structure, we did a time-resolved photoluminescence study (Figure 1d). The perovskite microcrystals on glass initially have an average lifetime of  $\tau_{av}$  = 5.01 ns. When the perovskite layer is deposited on ITO, we observe a lifetime reduction ( $\tau_{av} = 1.20$  ns) due to the dissociation of the electron and hole pairs in the perovskite-ITO junction. After we add P3HT layer on the perovskite microcrystals, the lifetime is further reduced ( $\tau_{\rm av} = 0.24~{\rm ns}$ ) due to the contribution of the P3HT-perovskite junction toward charge dissociation. Therefore, both heterojunctions (i.e., perovskite-ITO and P3HT-perovskite) contribute to the charge dissociation.

## 2.2. The Optoelectronic and Biological Properties of the Biointerface

To investigate the optoelectronic performance of the biointerface, the photocurrent was measured for different light intensities, wavelengths, and stability in an aqueous environment by using an electrophysiology amplifier. Artificial cerebrospinal fluid (aCSF), which mimics a similar electrophysiological condition for patch clamp studies, is used for the photocurrent measurements (Figure 3a). The transient behavior of the biointerface has near infrared photoresponse due to absorption by the surface states of the perovskite microcrystals (Figure 3b).[22,30] The biointerface shows a linear response to the light illumination (Figure 3c), and a photocurrent of ≈1.0 nA can be induced at a relatively low-intensity level of 100  $\mu$ W cm<sup>-2</sup> at 630 nm, which shows the effective photovoltaic performance of the biointerface. Here, the photogenerated electrons in the perovskite move to the external circuit through the ITO substrate and holes are directed toward the solution interface of the biointerface. Figure 3d also shows the photocurrent response for different wavelengths from blue to near-IR, and since the bandgap of the perovskite is 1.49 eV, the biointerface shows high photocurrent in the visible region below its bandgap energy. In comparison with the carriers in the sub-bandgap states, the interband transitions show a stronger photocurrent response. Moreover, to confirm the role of perovskite in the biointerface we checked the effect of the photocurrent generated by P3HT and PDMS:P3HT layers by measuring the photocurrents in ITO/PDMS:P3HT and ITO/P3HT/PDMS:P3HT structures, respectively. We observed negligible photocurrent levels for ITO/PDMS:P3HT and ITO/P3HT/PDMS:P3HT photoelectrodes in comparison to ITO/Perov/P3HT and ITO/ Perov/P3HT/PDMS:P3HT photoelectrodes (Figure S3, Supporting Information).

The stability of the biointerface was investigated for a period of 1 week in a cell culture medium under incubation condition (Figure 3d), and it showed only a 24% decrease of the photocurrent level after one week relative to its initial

www.advmatinterfaces.de

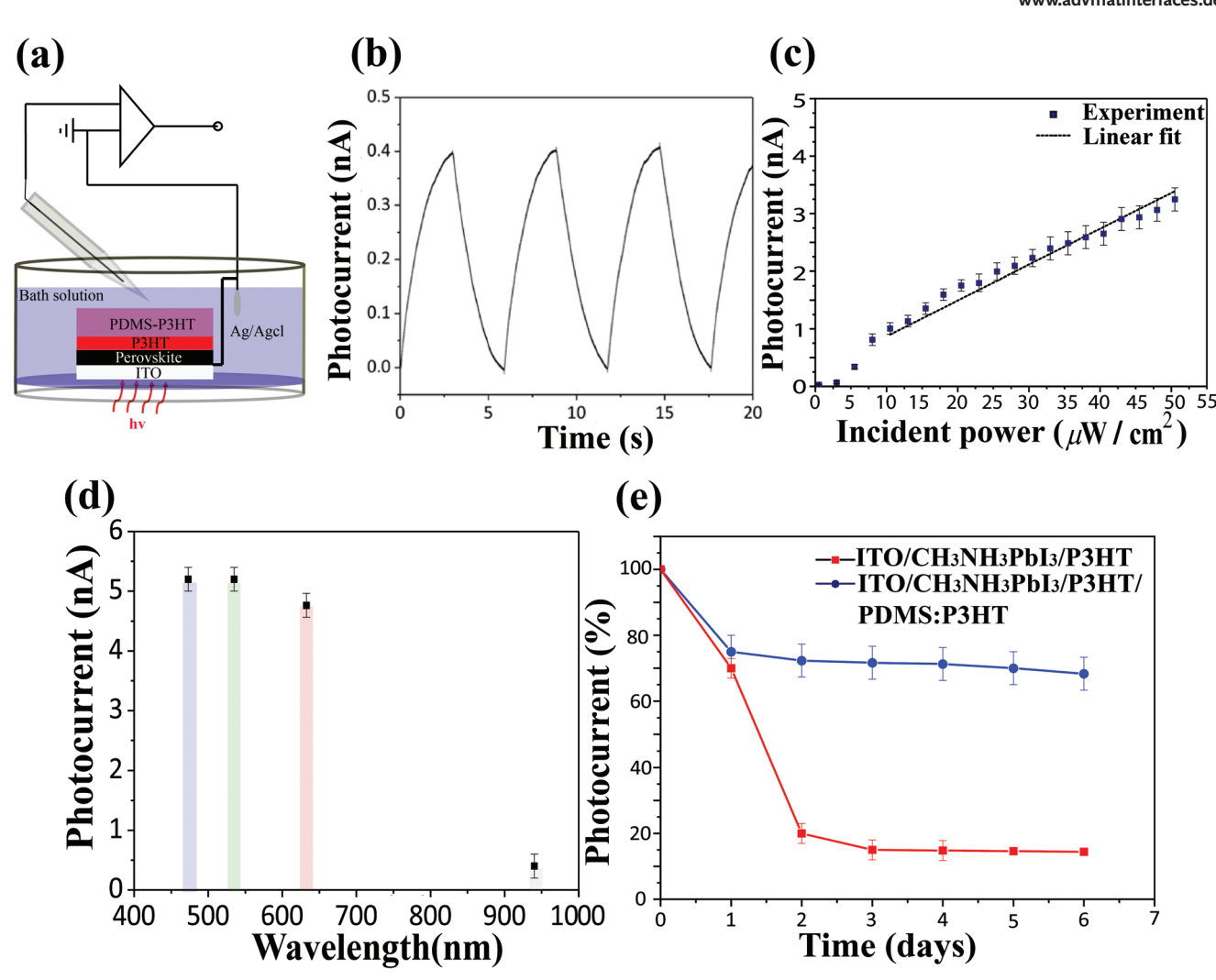


Figure 3. a) Schematic of the set-up for the photocurrent measurement. A patch pipette is positioned in close proximity to the P3HT surface and a patch-clamp amplifier is used to record photocurrents generated via light illumination. Light response of the biointerface (ITO/perovskite/P3HT/ PDMS:P3HT) under 630 nm light illumination. b) Near-IR (light pulse-width of 3 s, wavelength – 950 nm, light intensity – 100 μW cm<sup>-2</sup>) photocurrent response of the biointerface (ITO/perovskite/P3HT/P3HT:PDMS) in aCSF electrophysiology medium. c) Photocurrent versus input light intensity (light pulse width -3 s), which was fitted with a linear relation between 7.5 and 50  $\mu$ W cm<sup>-2</sup>. d) Photocurrent response of the biointerface at different input wavelengths of light having the intensity of 100 μW cm<sup>-2</sup> with light pulse of 3 s. Data are presented as mean value with the standard deviation (SD). e) Photocurrent stability (for n = 3 samples) of the biointerface and ITO/perovskite/P3HT in aCSF medium. The absolute photocurrent (measured with illumination at 630 nm, 50  $\mu$ W cm<sup>-2</sup>) on 0th day is 5.2 and 3.2 nA for ITO/perovskite/P3HT and the biointerface, respectively. Data are presented as mean value with the standard deviation (SD).

value. Depending on the cell type, hundreds of picoamperes are sufficient to stimulate the neurons, and even after this decrease, the biointerface can offer effective stimulation of neurons. Hence, this confirms that the biointerface is functional and is able to generate effective bioelectrical response after 1 week in biological environments. As control groups, we also investigated the perovskite film on ITO substrate, and in a few seconds the perovskite was dissolved in the aqueous environment (Figure S1, Supporting Information). As another control group, perovskite microcrystals and P3HT hybrid (without PDMS:P3HT coating) shows a six-fold decrease in photocurrent level after 1 week in comparison with its initial value. Hence, both the microcrystal formation and the polymeric layer of PDMS:P3HT layer enabled a drastic enhancement of perovskite stability in the cell medium.

Adv. Mater. Interfaces 2019, 6, 1900758

In addition to the stability in an aqueous environment, the biointerface requires simultaneous satisfaction of biocompatibility and safe photostimulation of neurons. Initially, we investigate the biocompatibility of the photoelectrode on cell viability using 3-(4,5-dimethylthiazol-2-yl)-2,5-diphenyl tetrazolium bromide (MTT) assay and apoptosis assay by fluorescence microscopy. We used different thicknesses of the PDMS:P3HT layer on top of perovskite/P3HT layer and performed the MTT assay experiment to confirm the biocompatibility of the biointerface (Figure 4a). It is observed that SH-SY5Y cells grown either on the biointerface or ITO (used as control) had comparable cell viability for the biointerface with 200 µm PDMS:P3HT using MTT assay. Therefore, 200 µm PDMS:P3HT is a good thickness to ensure the critical property of biocompatibility for the biointerface. Moreover, the nucleus and cytoplasm of the

ADVANCED MATERIALS

www.advmatinterfaces.de

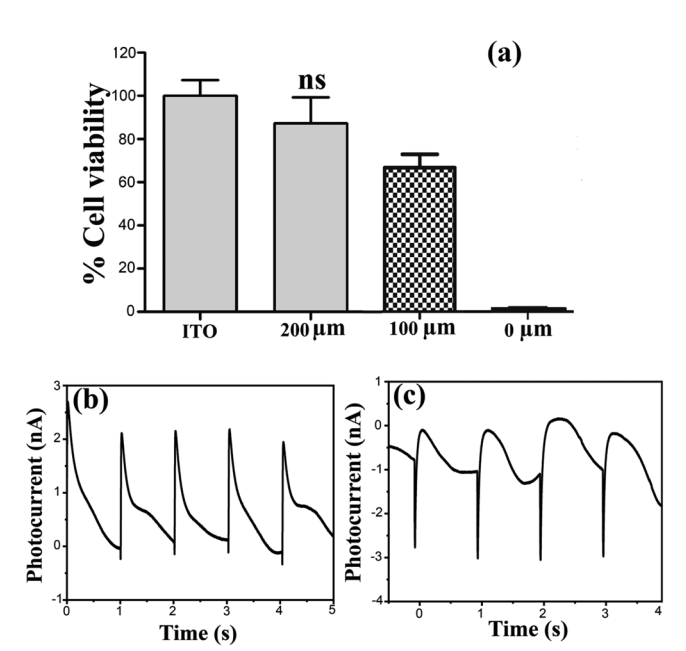


**Figure 4.** a) The cell viability assessment of biointerfaces with different thicknesses of the PDMS:P3HT layer on the SH-SY5Y cell line. The effect of the biointerfaces on metabolic activity of SH-SY5Y cells assessed by MTT. Data are presented in a column graph plotting the mean with the standard error of the mean (SEM). b) Photocurrent versus time for Faradaic biointerface under illumination of 10 ms light pulses with an intensity of 1 mW cm<sup>-2</sup>. c) Photocurrent versus time for capacitive biointerface under illumination of 10 ms light pulses with an intensity of 1 mW cm<sup>-2</sup>.

SH-SY5Y cells were grown on the biointerface and ITO, were stained by 4,6-diamidino-2-phenylindole, dihydrochloride (DAPI) and beta-III-Tubulin to assess the integrity of the cells, respectively (Figure S4, Supporting Information). Results showed that cells on both samples had comparable number of the stained cells, which suggested that biointerface had no toxic effect on the cells (Figure S5, Supporting Information). Additionally, the number of the apoptotic cells was determined on the both substrates by measuring the cleaved caspase 3 (CC3). The ratio of CC3+/DAPI+ number in the apoptotic cells were statistically not significant on both biointerface and ITO control substrates (Figure S5, Supporting Information). Collectively, all these results suggested that biointerface did not exhibit any toxicity on SH-SY5Y cells and allow us to perform further studies.

For safe photostimulation, capacitive charge-transfer mechanism is more preferred<sup>[31]</sup> for neural interfaces. In the ITO/ CH<sub>3</sub>NH<sub>3</sub>PbI<sub>3</sub>/P3HT/PDMS:P3HT biointerface, a strong Faradaic contribution is observed in addition to a weaker capacitive current (Figure 4b). In principle, according to the energy band diagram, a capacitive current is expected to be observed, but the voids present at perovskite thin film in microcrystals is considered as a main reason for the Faradaic leakage. To decrease the Faradaic contribution, we optimized the perovskite thin films by using multilayer spin-coating of precursor solution while keeping the thickness constant (Figure S2, Supporting Information). Formation of multilayers of the perovskite thin film enabled to reduce the leakage path. The photocurrent is measured for modified biointerface under similar condition and enhanced capacitive photocurrent along with Faradaic component is

observed at even low level of light-intensity (Figure 4c). Hence, we observed the reduction of Faradaic current through optimization of perovskite active thin film, which appears to be a suitable biointerface for photostimulation of neurons.

#### 2.3. Neuronal Activity at the Biointerface

We investigated the light activation of SH-SY5Y cells on the biointerface in a wireless and freestanding mode by using the calcium imaging. During the calcium imaging the excitation pulse of 1.5 ms at 552 nm with light intensity of 24 mW cm<sup>-2</sup> is applied (at the time of 19.09 s), which leads a sudden jump to the maximum calcium signal level due to effective photostimulation and decays after this excitation to its ground level. In fact, the probe light (488 nm) with light intensity of 8 mW cm<sup>-2</sup> that optically pumps the calcium tracker dye can also partially absorbed by the perovskite due to its wide photoabsorption window and leads an increasing calcium activity, which is observable until the excitation pulse. The result shown in Figure 5 represents the best calcium activity. However, the Ca imaging activity has confirmed for n = 12 biointerfaces for the repeatability of the experiment (Figure S6, Supporting Information). As a control group, ITO-coated glass substrates showed no calcium activity (Figure S7, Supporting Information) under the same light activation condition. To investigate the contribution of the photothermal effect, we calculated the possible temperature change, which is induced by the light source during calcium imaging.<sup>[32]</sup> The temperature change is less than 0.01 °C (see Supporting Information for the calculations), which is not enough for cell stimulation. For photothermal excitation at least several degrees of temperature change are required,[33] hence we consider that the thermal change is not responsible for photostimulation of the cells. Hence, the induction of calcium influx shows effective photostimulation of cells by the biointerface.

## 3. Conclusions

In conclusion, an organohalide perovskite is used for the development of a neural interface, which enables photoactivation of neuronal cells. High light sensitivity of the perovskite is the key property for a powerless and wireless stimulation. Advantageously long diffusion length and lifetime of the photon-induced charge carriers of perovskite can enable directional control of the carriers for the designated charge transfer mechanism. But, this can be a disadvantage in terms of resolution, which can be also solved by pixilation of the photoactive substrate. Furthermore, the photon-to-electron conversion capability in near IR can be advantageous for in vivo applications, where light has high-level of penetration into the tissue in the biological window. In this way, the interface application as a neural prosthetic device can be widen for a variety of in vivo applications such as brain or heart. Moreover, tuning energy bandgap of MAPbX<sub>3</sub> over the whole visible spectral range by adjusting the halide composition is a key advantage. In addition, the ability of operating in both narrowband and broadband regimes enable spectral control

21967350, 2019, 17, Downloaded from https://onlinelibrary.wiley.com/doi/10.1002/admi.201900758 by Egyptian National Sti. Network (Enstinet),

Wiley Online Library on [08/03/2023]. See the Terms

nelibrary.wiley.com/terms-and-conditions) on Wiley Online Library for rules of use; OA articles are governed by the applicable Creative Commons License

www.advmatinterfaces.de

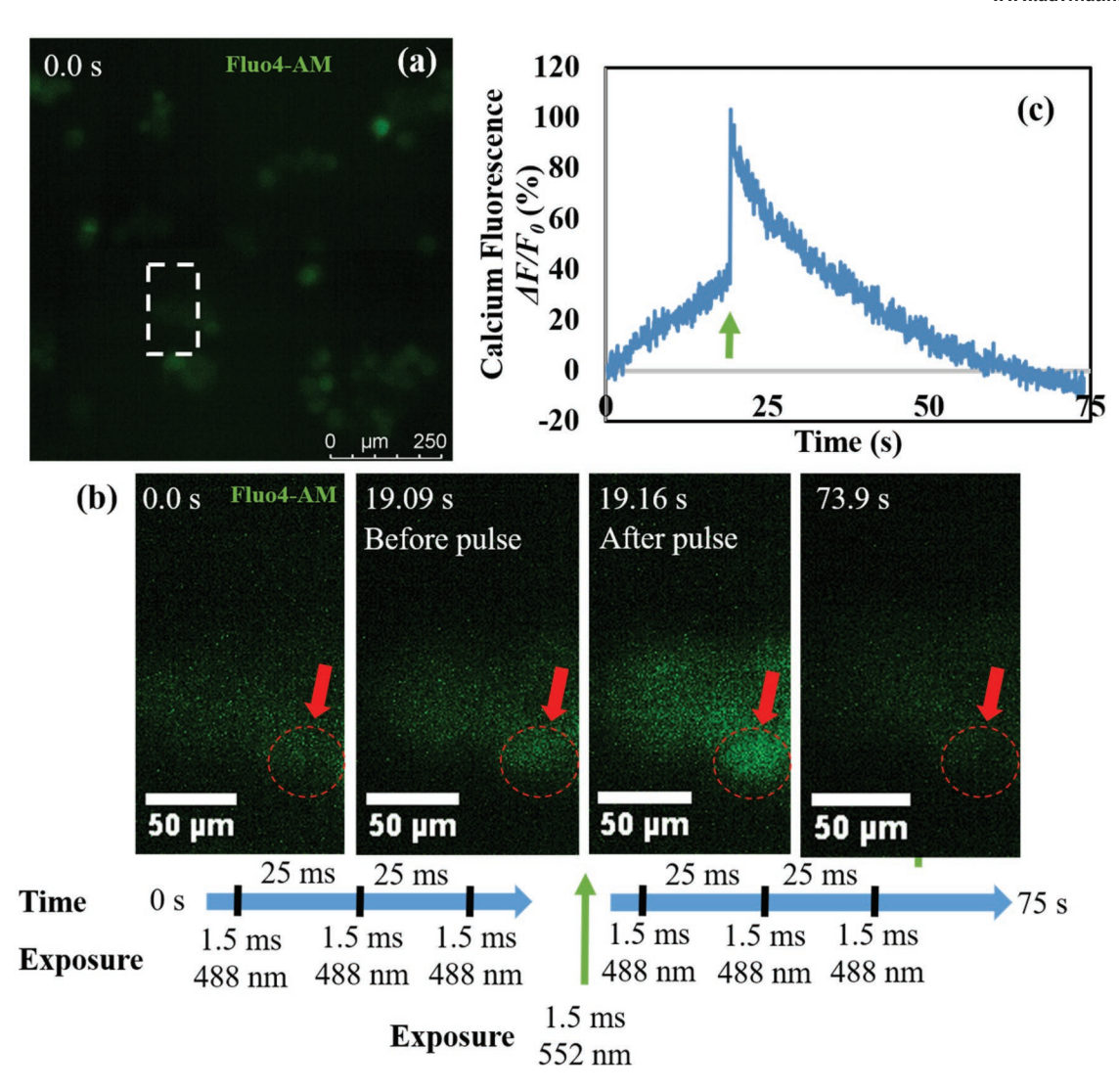


**Figure 5.** a) Fluo4-AM (green) labeled SH-SY5Y cells at time zero, image obtained by capturing FITC-conjugated Fluo4-AM with 1.5 ms exposure time of light illuminated with 488 nm wavelength. b) Schematic overview of time lapse calcium imaging. After time lapse series of calcium imaging with a capturing interval of 25 ms for 19.09 s, a single light pulse of 1.5 ms at 552 nm was exposed to the cells and immediately calcium imaging was continued until 75 s. Selected region of interest shows depolarization of a cell over time circled and indicated by a red arrow. Notice the increased calcium signal after a pulse of 1.5 ms at 552 nm at 19.16 s, which is also indicated by the green arrow in its subsequent calcium fluorescence peak. c) Calcium fluorescence  $\Delta F/F_0$  (%) versus time shows a spike immediately after 552 nm light pulse.

for retinal prosthesis. Moreover, P3HT and PDMS layer not only reduced the toxicity level of the hybrid, but also improved the stability of the perovskite in the neural cell medium, though toxicity of the perovskite has been so far considered as a major concern. Since there exists already a significant effort on lead-free and stable perovskite-based optoelectronics, in conjunction with new perovskite materials we believe that this study may open a new horizon for perovskite-based biomedical technologies.

## 4. Experimental Section

Biointerface Fabrication: ITO-coated glass substrates (Ossila) were cleaned in a sonication bath by using the following procedure: the glasses were dipped into a 10% NaOH solution (in distilled water),

washed in hot water, rinsed 2% Hellmanex in hot distilled water, rinsed in hot water, rinsed in cold isopropanol (IPA), and dried with nitrogen. Then, UV-ozone clean was used for the substrates before coating steps. Methylammonium iodide (Ossila, 99.9%), lead (II) iodide (Aldrich, 99.9%), and isopropanol were used to synthesize perovskite microcrystals.  $1 \times 10^{-3}$  M MAI was dissolved in 1.5 mL IPA and then  $1\times 10^{-3}~\text{M}$  PbI $_2$  was mixed for making 0.67 M perovskite suspension. The perovskite solution was spin-coated on top of the ITO glasses at 2000 rpm. Rr-P3HT (Sigma-Aldrich) with a regioregularity of 99.5% and toluene of 99.9% purity were mixed to make the P3HT solution. 30 mg  $\mathrm{mL}^{-1}$  concentration of the P3HT was spin-coated at 3000 rpm to make a thin layer of P3HT film on top of the perovskite layer. For making PDMS:P3HT composite layer, 10 g of PDMS SYLGARD 184 Elastomer was mixed with 2 g of SYLGARD 184 curing agent and 1 mL P3HT solution (20 mg mL in toluene). Then, it was stirred for 3 min until bubbles appeared in the mixture. After that, the mixture was degassed in the vacuum desiccator for 20 min until the bubbles were completely disappeared. The PDMS:P3HT



www.advmatinterfaces.de

mixture was coated on the P3HT layer by using doctor blade technique. The mixture was heated at 60  $^{\circ}$ C for 6 h for completion of curing process.

Cell Culture and Cell Seeding: SH-SY5Y cell line was cultured in Dulbecco's modified Eagle's medium (DMEM, Gibco 21969-035) supplied with 10% heat-inactivated fetal bovine serum (FBS, Gibco 10500), 1% L-glutamine (Gibco 25030-081), and 1% penicillin–streptomycin (Gibco 15240-062). The cells were maintained at 37 °C in a 5% CO $_2$  and 85% humidified incubator. The cells were subcultured by supplying with fresh medium with a subculture ratio of 1:3. Before cell seeding, biointerfaces were sterilized as follows: substrates were washed with 70% ethanol, rinsed by dH $_2$ O and air dried. For surface sterilization, substrates were exposed to UVC lamp for 30 min. For cell seeding, the cells were cultured to 90% confluency and detached from the plate by trypsinization. Detached cells were transferred onto substrates in a fresh complete medium.

Cell Viability Test (MTT Assay): Biointerfaces were cut into  $0.40~\text{cm} \times 0.40~\text{cm}$  pieces and sterilized as follows: samples were treated with 70% ethanol and air dried. Following ethanol treatment, they were exposed to UV-lamp for 30 min before cell seeding. Sterilized biointerfaces were placed into a sterile 96-well plate. SH-SY5Y cells were seeded to each well in 100 µL DMEM medium containing 10% FBS with a concentration of  $1 \times 10^4$  cells per well. To allow cell adherence, the samples was incubated at 37 °C in a 5% CO2 incubator for 48 h. Then, growth medium was replaced with DMEM containing 1 mg mL<sup>-1</sup> (3-(4,5-dimethylthiazol-2-yl)-2,5-diphenyltetrazolium solution and further incubated for 4 h to allow formazan salt formation. Finally, the MTT:DMEM solution was removed and formazan salts were dissolved in 200  $\mu L$  EtOH:DMSO mixture. The optical density (OD) was measured at 600 nm with BioTek Synergy H1 Microplate Reader. The relative cell viability was calculated as viability = (OD<sub>sample</sub>/ OD<sub>control</sub>) × 100. OD<sub>sample</sub> was obtained from biointerfaces, and OD<sub>control</sub> was obtained from ITO controls.

Fluorescence Imaging: In order to investigate the morphology and activation of SH-SY5Y grown on biointerfaces, cells were seeded on substrates and allowed to attach for 24 h incubation at 37 °C in a 5% CO<sub>2</sub> incubator. After 24 h of incubation, cells were fixed by 30 min incubation with 4% paraformaldehyde at room temperature; and washed three times with Dulbecco's phosphate-buffered saline (DPBS). Subsequently, cells were permeabilized with 0.1% Triton X-100 for 5 min and washed again three times with DPBS. Then, the cells were stained for 1.5 h at 37 °C (1:250 dilution) with mouse anti-beta-III-tubulin primary antibody (Abcam, Ab78078) and rabbit anticleaved caspase-3 primary antibody (Cellsignal, #9664). After washing with DPBS, cells were stained with a mixture of FITC anti-mouse (1:250, Jackson ImmunoResearch, 115-095-003) and Cy3 antirabbit secondary antibodies (1:250, Jackson ImmunoResearch,  $\dot{1}$ 1-165-003) for 1.5 h at 37 °C. Finally, samples were stained with DAPI and mounted for fluorescent imaging. Imaging was performed with DMi-8 epifluorescent inverted microscope (Leica, Germany).

Calcium Imaging: The set of experiments is performed to lead to neuronal depolarization through the activation of photoactive material and indirectly detect depolarization with calcium imaging. Calcium imaging was performed with acetoxy-methyl-ester Fura-4 (Fluo-4 AM) which is a calcium-chelating ester. When incubated, Fluo-4AM diffuses across the cell membrane, de-esterifies in the cell and stays in the neuron. Calcium ions cause intramolecular conformational changes in Fluo-4AM that leads to a change in the emitted fluorescence. The excitation wavelength for Fluo-4AM-FITC conjugated is 494 nm and emission wavelength is 516 nm. With the increased intracellular calcium, the emitted fluorescent light intensity increases and can be detected with appropriate filter sets on the epiflourescent microscope. Briefly, SH-SY5Y cells were seeded on photoactive material-coated glass substrates (n = 3) and noncoated control glass substrates (n = 3). The cells were incubated for 24 h at 37 °C and 5% CO<sub>2</sub> in neurobasal medium (Invitrogen) supplemented with B27 (Gibco), L-glutamine (Gibco), and penicillin/streptomycin (Gibco), hereafter referred as complete neurobasal medium. Subsequently, with a final concentration of 5  $\times$  10<sup>-6</sup> M, Fluo-4AM (Gibco) was added to the medium and incubated for 60 min at 37 °C and 5% CO2 in dark. Then, extracellular remaining Fluo-4AM was removed by changing medium into Fluo-4AM free complete neurobasal medium. Subsequently, after an incubation period of 30 min, the cells were traced with the DMi8 fluorescent inverted microscope (Leica, Germany) for calcium dynamics. Light pulse exposure was set as a single pulse of 1.5 ms at 552 nm during serial calcium imaging. Exposure time and image acquisition was kept equal between all samples. Captured time-laps TIF-file series were analyzed using Image] (NIH) for fluorescence intensity ratio changes ( $\Delta F/F_0$ ) of cells marked with the ROI Manager. Multimeasure option was used to measure the time-lapse fluorescent mean intensity values from which background noise was subtracted yielding  $\Delta F$ . Then,  $F_0$  was set as the starting fluorescent intensity at time 0. Final fluorescence ratio change was calculated as percentage of  $\Delta F/F_0$ . A resting intracellular calcium concentration corresponds to  $\Delta F/F_0 = 1$  and upward deflections indicate an increase in intracellular calcium concentration and hence depolarization. Moreover, the effect of 488 and 552 nm exposure on maximum calcium fluorescence peaks and peak onset times was compared.

Photocurrent and Photostimulation: Both photostimulation and photocurrent measurements were performed by using light-emitting diodes at different wavelengths (see Figure S8 of the Supporting Information for the spectrum of the LEDs operating in the visible range). For the near-IR stimulation IR LED operating at 950 nm (Osram Opto SFH 4248) was used. The power per unit area was measured with a power meter (Newport 843-R). To reduce the noise level a Faraday cage covering the whole electrophysiology system was used.

# **Supporting Information**

Supporting Information is available from the Wiley Online Library or from the author

## Acknowledgements

M.M.A. and S.B.S. contributed equally to the work. This project received funding from the European Research Council (ERC) under the European Union's Horizon 2020 Research and Innovation Programme (Grant Agreement No. 639846). The authors thank M. Barış Yağcı for scanning electron microscopy measurements, Ceren Yılmaz Akkaya for XRD measurements, and Koç University Surface Science and Technology Center (KUYTAM) for providing the SEM and XRD measurement infrastructure. The authors thank to Aşkın Kocabaş from Koç University and Vishnu Nair from University of Chicago for his comments about Ca imaging experiment. The authors gratefully acknowledge use of the services and facilities of the Koç University Research Center for Translational Medicine (KUTTAM), funded by the Republic of Turkey Ministry of Development. The content is solely the responsibility of the authors and does not necessarily represent the official views of the Ministry of Development.

# **Conflict of Interest**

The authors declare no conflict of interest.

#### **Keywords**

biointerface, calcium imaging, electrophysiology, neural stimulation, perovskites, photostimulation

Received: April 30, 2019 Revised: June 13, 2019 Published online: July 11, 2019



www.advmatinterfaces.de

- [1] K. Kampasi, E. Stark, J. Seymour, K. Na, H. G. Winful, G. Buzsáki, K. D. Wise, E. Yoon, *Sci. Rep.* **2016**, *6*, 30961.
- [2] a) R. Chen, A. Canales, P. Anikeeva, Nat. Rev. Mater. 2017, 2, 16093;
  b) D. Borton, S. Micera, J. d. R. Millán, G. Courtine, Sci. Transl. Med. 2013, 5, 210rv2.
- [3] W. R. Patterson, S. Yoon-Kyu, C. W. Bull, I. Ozden, A. P. Deangellis, C. Lay, J. L. McKay, A. V. Nurmikko, J. D. Donoghue, B. W. Connors, IEEE Trans. Biomed. Eng. 2004, 51, 1845.
- [4] a) N. A. Kotov, J. O. Winter, I. P. Clements, E. Jan, B. P. Timko, S. Campidelli, S. Pathak, A. Mazzatenta, C. M. Lieber, M. Prato, R. V. Bellamkonda, G. A. Silva, N. W. S. Kam, F. Patolsky, L. Ballerini, Adv. Mater. 2009, 21, 3970; b) H. Bahmani Jalali, M. Mohammadi Aria, U. M. Dikbas, S. Sadeghi, B. Ganesh Kumar, M. Sahin, I. H. Kavakli, C. W. Ow-Yang, S. Nizamoglu, ACS Nano 2018, 12, 8104.
- [5] J. N. Fayad, S. R. Otto, R. V. Shannon, D. E. Brackmann, *Proc. IEEE* 2008, 96, 1085.
- [6] a) E. Zrenner, Sci. Transl. Med. 2013, 5, 210ps16; b) K. Mathieson, J. Loudin, G. Goetz, P. Huie, L. Wang, T. I. Kamins, L. Galambos, R. Smith, J. S. Harris, A. Sher, D. Palanker, Nat. Photonics 2012, 6, 391
- [7] D. Ghezzi, M. R. Antognazza, R. Maccarone, S. Bellani, E. Lanzarini, N. Martino, M. Mete, G. Pertile, S. Bisti, G. Lanzani, F. Benfenati, Nat. Photonics 2013, 7, 400.
- [8] L. Wang, K. Mathieson, T. I. Kamins, J. D. Loudin, L. Galambos, G. Goetz, A. Sher, Y. Mandel, P. Huie, D. Lavinsky, J. S. Harris, D. V. Palanker, J. Neural Eng. 2012, 9, 046014.
- [9] a) M. Capogrosso, J. Gandar, N. Greiner, E. M. Moraud, N. Wenger, P. Shkorbatova, P. Musienko, I. Minev, S. Lacour, G. Courtine, J. Neural Eng. 2018, 15, 026024; b) M. Capogrosso, T. Milekovic, D. Borton, F. Wagner, E. M. Moraud, J.-B. Mignardot, N. Buse, J. Gandar, Q. Barraud, D. Xing, E. Rey, S. Duis, Y. Jianzhong, W. K. D. Ko, Q. Li, P. Detemple, T. Denison, S. Micera, E. Bezard, J. Bloch, G. Courtine, Nature 2016, 539, 284.
- [10] T. Wichmann, M. R. DeLong, Neuron 2006, 52, 197.
- [11] a) A. T. Young, N. Cornwell, M. A. Daniele, Adv. Funct. Mater. 2018, 28, 1700239; b) P. Fattahi, G. Yang, G. Kim, M. R. Abidian, Adv. Mater. 2014, 26, 1846.
- [12] J. F. Maya-Vetencourt, D. Ghezzi, M. R. Antognazza, E. Colombo, M. Mete, P. Feyen, A. Desii, A. Buschiazzo, M. Di Paolo, S. Di Marco, F. Ticconi, L. Emionite, D. Shmal, C. Marini, I. Donelli, G. Freddi, R. Maccarone, S. Bisti, G. Sambuceti, G. Pertile, G. Lanzani, F. Benfenati, Nat. Mater. 2017, 16, 681.
- [13] a) K. Song, J. H. Han, T. Lim, N. Kim, S. Shin, J. Kim, H. Choo, S. Jeong, Y.-C. Kim, Z. L. Wang, J. Lee, Adv. Healthcare Mater. 2016, 5, 1572; b) H. Lorach, G. Goetz, R. Smith, X. Lei, Y. Mandel, T. Kamins, K. Mathieson, P. Huie, J. Harris, A. Sher, D. Palanker, Nat. Med. 2015, 21, 476; c) L. Bareket-Keren, Y. Hanein, Int. J. Nanomed. 2014, 9 Suppl 1, 65; d) E. Zrenner, Nat. Photonics 2012, 6, 344.
- [14] a) L. Bareket, N. Waiskopf, D. Rand, G. Lubin, M. David-Pur, J. Ben-Dov, S. Roy, C. Eleftheriou, E. Sernagor, O. Cheshnovsky, U. Banin, Y. Hanein, Nano Lett. 2014, 14, 6685; b) K. Lugo, X. Miao, F. Rieke, L. Y. Lin, Biomed. Opt. Express 2012, 3, 447; c) M. A. Malvindi, L. Carbone, A. Quarta, A. Tino, L. Manna, T. Pellegrino, C. Tortiglione, Small 2008, 4, 1747; d) J. O. Winter, N. Gomez, B. A. Korgel, C. E. Schmidt, Quantum dots for Electrical Stimulation of Neural Cells, Vol. 5705, SPIE, Bellingham, WA 2005.
- [15] a) P. Bazard, R. D. Frisina, J. P. Walton, V. R. Bhethanabotla, *Sci. Rep.* 2017, 7, 7803; b) S. Yoo, R. Kim, J.-H. Park, Y. Nam, *ACS Nano* 2016, 10, 4274.
- [16] a) K. Yang, J. Y. Oh, J. S. Lee, Y. Jin, G. E. Chang, S. S. Chae,
  E. Cheong, H. K. Baik, S. W. Cho, *Theranostics* 2017, 7, 4591;
  b) Y.-S. Hsiao, Y.-H. Liao, H.-L. Chen, P. Chen, F.-C. Chen, ACS
  Appl. Mater. Interfaces 2016, 8, 9275; c) O. S. Abdullaeva, M. Schulz,

- F. Balzer, J. Parisi, A. Lützen, K. Dedek, M. Schiek, Langmuir 2016, 32, 8533; d) V. Benfenati, N. Martino, M. R. Antognazza, A. Pistone, S. Toffanin, S. Ferroni, G. Lanzani, M. Muccini, Adv. Healthcare Mater. 2014, 3, 306; e) N. Martino, D. Ghezzi, F. Benfenati, G. Lanzani, M. R. Antognazza, J. Mater. Chem. B 2013, 1, 3768; f) V. Benfenati, S. Toffanin, S. Bonetti, G. Turatti, A. Pistone, M. Chiappalone, A. Sagnella, A. Stefani, G. Generali, G. Ruani, D. Saguatti, R. Zamboni, M. Muccini, Nat. Mater. 2013, 12, 672; g) D. Ghezzi, M. R. Antognazza, M. Dal Maschio, E. Lanzarini, F. Benfenati, G. Lanzani, Nat. Commun. 2011, 2, 166.
- [17] T. C. Sum, N. Mathews, Energy Environ. Sci. 2014, 7, 2518.
- [18] D. Shi, V. Adinolfi, R. Comin, M. Yuan, E. Alarousu, A. Buin, Y. Chen, S. Hoogland, A. Rothenberger, K. Katsiev, Y. Losovyj, X. Zhang, P. A. Dowben, O. F. Mohammed, E. H. Sargent, O. M. Bakr, *Science* 2015, 347, 519.
- [19] a) Q. Dong, Y. Fang, Y. Shao, P. Mulligan, J. Qiu, L. Cao, J. Huang, Science 2015, 347, 967; b) S. D. Stranks, G. E. Eperon, G. Grancini, C. Menelaou, M. J. P. Alcocer, T. Leijtens, L. M. Herz, A. Petrozza, H. J. Snaith, Science 2013, 342, 341.
- [20] a) C. Zuo, H. J. Bolink, H. Han, J. Huang, D. Cahen, L. Ding, Adv. Sci. 2016, 3, 1500324; b) B.-w. Park, B. Philippe, S. M. Jain, X. Zhang, T. Edvinsson, H. Rensmo, B. Zietz, G. Boschloo, J. Mater. Chem. A 2015, 3, 21760; c) S. A. Kulkarni, T. Baikie, P. P. Boix, N. Yantara, N. Mathews, S. Mhaisalkar, J. Mater. Chem. A 2014, 2, 9221.
- [21] a) C. Xie, P. You, Z. Liu, L. Li, F. Yan, Light: Sci. Appl. 2017, 6, e17023; b) W. Wang, D. Zhao, F. Zhang, L. Li, M. Du, C. Wang, Y. Yu, Q. Huang, M. Zhang, L. Li, J. Miao, Z. Lou, G. Shen, Y. Fang, Y. Yan, Adv. Funct. Mater. 2017, 27, 1703953; c) N. Arora, M. I. Dar, A. Hinderhofer, N. Pellet, F. Schreiber, S. M. Zakeeruddin, M. Grätzel, Science 2017, 358, 768; d) M. I. Saidaminov, M. A. Haque, M. Savoie, A. L. Abdelhady, N. Cho, I. Dursun, U. Buttner, E. Alarousu, T. Wu, O. M. Bakr, Adv. Mater. 2016, 28, 8144; e) K. Pandey, M. Chauhan, V. Bhatt, B. Tripathi, P. Yadav, M. Kumar, RSC Adv. 2016, 6, 105076; f) G. Maculan, A. D. Sheikh, A. L. Abdelhady, M. I. Saidaminov, M. A. Haque, B. Murali, E. Alarousu, O. F. Mohammed, T. Wu, O. M. Bakr, J. Phys. Chem. Lett. 2015, 6, 3781; g) H. S. Jung, N.-G. Park, Small 2015, 11, 10.
- [22] Q. Lin, A. Armin, P. L. Burn, P. Meredith, Laser Photonics Rev. 2016, 10, 1047.
- [23] J. Ding, H. Fang, Z. Lian, J. Li, Q. Lv, L. Wang, J.-L. Sun, Q. Yan, CrystEngComm 2016, 18, 4405.
- [24] D. Wang, M. Wright, N. K. Elumalai, A. Uddin, Sol. Energy Mater. Sol. Cells 2016, 147, 255.
- [25] a) S. Kundu, T. L. Kelly, Mater. Chem. Front. 2018, 2, 81; b) M. Park, J.-S. Park, I. K. Han, J. Y. Oh, J. Mater. Chem. A 2016, 4, 11307; c) T. Gatti, S. Casaluci, M. Prato, M. Salerno, F. Di Stasio, A. Ansaldo, E. Menna, A. Di Carlo, F. Bonaccorso, Adv. Funct. Mater. 2016, 26, 7443; d) M. Zhang, M. Lyu, H. Yu, J.-H. Yun, Q. Wang, L. Wang, Chem. Eur. J. 2015, 21, 434; e) J. Xiao, J. Shi, H. Liu, Y. Xu, S. Lv, Y. Luo, D. Li, Q. Meng, Y. Li, Adv. Energy Mater. 2015, 5, 1401943.
- [26] G. Tullii, A. Desii, C. Bossio, S. Bellani, M. Colombo, N. Martino, M. R. Antognazza, G. Lanzani, Org. Electron. 2017, 46, 88.
- [27] a) L. Ferlauto, M. J. I. Airaghi Leccardi, N. A. L. Chenais, S. C. A. Gilliéron, P. Vagni, M. Bevilacqua, T. J. Wolfensberger, K. Sivula, D. Ghezzi, Nat. Commun. 2018, 9, 992; b) A. Shit, A. K. Nandi, Phys. Chem. Chem. Phys. 2016, 18, 10182; c) Y. Zhang, W. Liu, F. Tan, Y. Gu, J. Power Sources 2015, 274, 1224; d) M. Seetharaman S, P. Nagarjuna, P. N. Kumar, S. P. Singh, M. Deepa, M. A. G. Namboothiry, Phys. Chem. Chem. Phys. 2014, 16. 24691.
- [28] a) B.-W. Park, B. Philippe, X. Zhang, H. Rensmo, G. Boschloo,
   E. M. J. Johansson, Adv. Mater. 2015, 27, 6806; b) V. Bhatt,
   M. Kumar, P. Yadav, M. Kumar, J.-H. Yun, Mater. Res. Bull. 2018, 99,





www.advmatinterfaces.de

- 79; c) J. Yu, X. Chen, Y. Wang, H. Zhou, M. Xue, Y. Xu, Z. Li, C. Ye, J. Zhang, P. A. van Aken, P. D. Lund, H. Wang, *J. Mater. Chem. C* **2016**, *4*, 7302.
- [29] A. Ummadisingu, M. Grätzel, Sci. Adv. 2018, 4, e1701402.
- [30] R. Dong, Y. Fang, J. Chae, J. Dai, Z. Xiao, Q. Dong, Y. Yuan, A. Centrone, X. C. Zeng, J. Huang, Adv. Mater. 2015, 27, 1912.
- [31] a) S. B. Srivastava, R. Melikov, M. M. Aria, U. M. Dikbas, I. H. Kavakali, S. Nizamoglu, *Phys. Rev. Appl.* **2019**, *11*, 044012;
- b) D. Rand, M. Jakešová, G. Lubin, I. Vebraité, M. David-Pur, V. Đerek, T. Cramer, N. S. Sariciftci, Y. Hanein, E. D. Głowacki, *Adv. Mater.* **2018**, *30*, 1707292.
- [32] T. C. Pappas, W. M. S. Wickramanyake, E. Jan, M. Motamedi, M. Brodwick, N. A. Kotov, Nano Lett. 2007, 7, 513.
- [33] S. Liang, F. Yang, C. Zhou, Y. Wang, S. Li, C. K. Sun, J. L. Puglisi, D. Bers, C. Sun, J. Zheng, Cell Biochem. Biophys. 2008, 53, 33.